University of Glasgow

Silicon nitride/silica quarter-wave stacks for low-thermal-noise mirror coatings

Huang-Wei Pan[1], Ling-Chi Kuo[1], Lin-An Chang[1], Shiuh Chao[1,*], Iain William Martin[2], Jessica Steinlechner[2,3], and Mark Fletcher[2]

[1]Institute of Photonics Technologies, National Tsing Hua University, Hsinchu 30013, Taiwan, R.O.C.
[2]SUPA, School of Physics and Astronomy, University of Glasgow, Glasgow G12 8QQ, Scotland
[3]Institut für Laserphysik and Zentrum für Optische Quantentechnologien, Universität Hamburg, Luruper Chaussee 149, Hamburg 22761, Germany

*Corresponding author e-mail: schao@ee.nthu.edu.tw

Abstract

This study investigated a multi-layer high reflector with new coating materials for next-generation laser interferometer gravitational wave detectors operated at cryogenic temperatures. We used the plasma-enhanced chemical vapor deposition method to deposit amorphous silicon nitride/silica quarter-wave high-reflector stacks and studied the properties pertinent to the coating thermal noise. Room- and cryogenic-temperature mechanical loss angles of the silicon nitride/silica quarter-wave bilayers were measured using the cantilever ring-down method. We showed, for the first time, that the bulk and shear loss angles of the coatings can be obtained from the cantilever ring-down measurement, and used the bulk and shear losses to calculate the coating thermal noise of silicon nitride/silica high-reflector coatings. The mechanical loss angle of the silicon nitride/silica bilayer is dispersive with a linear weakly positive frequency dependence, and hence, the coating thermal noise of the high reflectors showed a weakly positive frequency dependence in addition to the normal $1/\sqrt{f}$ dependence. The coating thermal noise of the silicon nitride/silica high-reflector stack is compared to the lower limit of the coating thermal noise of the end test mirrors of ET-LF, KAGRA, LIGO Voyager, and the directly measured coating thermal noise of the current coatings of Advanced LIGO. The optical absorption of the silicon nitride/silica high reflector at 1550 nm is 45.9 ppm. Using a multimaterial system composed of seven pairs of ion-beam-sputter deposited

1

Ti:Ta$_2$O$_5$/silica and nine pairs of silicon nitride/silica on a silicon substrate, the optical absorption can be reduced to 2 ppm that meets the specification of LIGO Voyager.

I. INTRODUCTION

After the first detection of gravitational waves from a binary black hole merger [1] by laser interferometer gravitational wave detectors and the recent observation of the complete evolution of a binary neutron star merger [2], gravitational-wave astronomy is moving forward at a fast pace. Next-generation laser interferometer gravitational wave detectors operated at cryogenic temperatures for higher sensitivity have been planned, i.e., Einstein-telescope low frequency (ET-LF) at 10 K [3] and LIGO Voyager at 120 K [4], or are already in construction, i.e., KAGRA at 20 K [5]. Reducing the cryogenic Brownian thermal noise of the mirror coating around the most sensitive frequency range ($\approx$ 100 Hz) is becoming particularly critical with the advances in the reduction of quantum noise using squeezed-light technologies [6,7].

A high-reflector (HR) dielectric coating is composed of pairs of high- and low-refractive-index films, each of one quarter-wave (QW) optical thickness, deposited alternately on a substrate. We previously reported [8] the use of silicon nitride films deposited via the plasma-enhanced chemical vapor deposition (PECVD) method for mirror coatings. The physical properties of the silicon nitride films vary with the composition of the films. We found that the properties of SiN$_{0.40}$H$_{0.79}$, such as its high refractive index, low optical absorption, and low mechanical loss, and in particular, the absence of a cryogenic mechanical loss peak, render it most suitable for mirror coatings. According to the criteria set for the thin-film materials for application as the mirror coatings of a laser interferometer gravitational wave detector [8,9], in this work, we pair the SiN$_{0.40}$H$_{0.79}$ film with a silica film, both deposited via PECVD and each of one QW optical thickness, to form the basic QW high-/low-refractive-index bilayer building unit of the HR coatings. Cryogenic- and room-temperature ($\approx$ 290 K) mechanical losses were measured and the Brownian coating thermal noise (CTN) was calculated, analyzed, and compared with the specifications of ET-LF, LIGO Voyager, KAGRA, and aLIGO. Hereafter, "silicon nitride" specifically refers to SiN$_{0.40}$H$_{0.79}$.

II. DEPOSITION AND BASIC PROPERTIES OF MATERIALS

Both silicon nitride and silica films were deposited by the PECVD method. The advantages of using PECVD over the conventional ion beam sputter (IBS) method include the ease of achieving large-area coating uniformity [8]. Precursors with pre-determined flow rates were fed into the reaction chamber together with the carrier gas to form plasma with free radicals. Chemical reactions occurred near the substrate held at an elevated temperature, and the products condensed on the substrate to form a film. The PECVD processes for depositing silicon nitride

and silica were described in the previous reports [8,10] and the process parameters are summarized in Table I.

TABLE I. PECVD process parameters: precursors, flow rate, carrier gas, substrate temperature, and total pressure for depositing silicon nitride and silica films. The RF power was 20 W at 13.56 MHz.

Material	Precursor (sccm)	Carrier gas (sccm)	Temp. (°C)	Press. (torr)
$SiN_{0.40}H_{0.79}$	SiH_4/NH_3 (45/15)	N_2 (980)	300	1
SiO_2	SiH_4/N_2O (8.5/710)	N_2 (161.5)	300	1

The refractive index n, extinction coefficient κ, stress, Young's modulus Y, Poisson's ratio σ and density ρ of the films were also presented in the previous reports [8,10-13] and they are summarized in Table II. The stresses of the silicon nitride and silica films are close in magnitude but opposite in sign, indicating that the multilayer stack is less susceptible to stress incompatibility and is hence mechanically stable. The refractive index difference between the two materials is larger than that of the conventional Ti:Ta_2O_5/silica QW stack as shown in Table II and VIII, indicating that fewer QW pairs are required to achieve the same level of transmittance and it is in favor of achieving lower CTN.

Multilayer QW stacks of silicon nitride/silica were deposited in the same PECVD chamber by switching the process parameters alternately between the conditions given in Table I. Deposition rates for each material were pre-determined—3.1 ± 0.2 Å/s for silicon nitride and 10.7 ± 0.2 Å/s for silica—and the thicknesses of the films were controlled using the deposition time. Thicknesses of the films were measured by using a transmission electron microscope and they were found to be within $\pm$ 2.5% and $\pm$ 1.0% of the designed values for silicon nitride and silica, respectively. The films were deposited on (001) silicon cantilevers. Cantilever samples with 1-,2-,3-,4-, and 8-pairs of silicon nitride/silica QW bilayers were deposited for the measurements of mechanical loss and the following analysis.

TABLE II. Basic material properties of silicon nitride and silica films deposited via PECVD.

Material	n (1064 nm)	n (1550 nm)	κ^a (1550 nm, 10^{-5})	Stress (MPa)	Y (GPa)	σ	ρ (g/cm^3)
$SiN_{0.40}H_{0.79}$ [8]	2.30 ± 0.01	2.28 ± 0.01	1.51 ± 0.09	120.2 ± 15.5	103.7 ± 5.6	0.25 [11]	2.00
SiO_2 [10]	1.45 ± 0.01	1.45 ± 0.01	0.75 ± 0.07	-158.2 ± 6.0	83.8 ± 1.3	0.17 [12]	2.17

^{a} κ for 1064 nm is not available.

III. THEORY

A. Coating thermal noise

The power spectral density of the Brownian coating thermal noise $S_x(f)$ was derived [13] from the fluctuation-dissipation theorem [14] as follows:

$$S_x(f) = \frac{4K_B T}{\pi f} \frac{U}{F_0^2} \phi(f),$$ (1)

where K_B is the Boltzman constant, T is the temperature, U is the maximum stored energy in the coating when a cyclic driving force with frequency f and amplitude F_0 is applied, and $\phi(f)$ is the mechanical loss angle of the coating.

The maximum stored energy U and the average energy dissipation per cycle $2\pi\phi U$ are composed of independent components from the bulk and shear motions as demonstrated by Hong et al. [16]. $\phi(f)$ and $S_x(f)$ were given as:

$$\phi(f) = \frac{U_B}{U} \phi_B(f) + \frac{U_S}{U} \phi_S(f),$$ (2)

$$S_x(f) = \frac{4K_B T}{\pi f} \left[\frac{U_B}{F_0^2} \phi_B(f) + \frac{U_S}{F_0^2} \phi_S(f) \right],$$ (3)

where U_B, U_S and $\phi_B(f)$, $\phi_S(f)$ are the maximum stored energies and the loss angles of the bulk and shear motion, respectively.

For a coating with one thin layer, the coefficients in the parenthesis of Eq. (3) are given as [15]:

$$\frac{U_B}{F_0^2} = \frac{d_c(1-2\sigma_c)}{3} \left[\frac{Y_c}{Y_s^2} \frac{(1-2\sigma_s)^2(1+\sigma_s)^2}{(1-\sigma_c)^2} + \frac{1}{Y_s} \frac{2(1-2\sigma_s)(1+\sigma_s)(1+\sigma_c)}{(1-\sigma_c)^2} + \frac{1}{Y_c} \frac{(1+\sigma_c)^2}{(1-\sigma_c)^2} \right] \times \frac{1}{\pi w_0^2},$$ (4)

$$\frac{U_S}{F_0^2} = \frac{2d_c}{3} \left[\frac{Y_c}{Y_s^2} \frac{(1-\sigma_c+\sigma_c^2)(1+\sigma_s)^2(1-2\sigma_s)^2}{(1-\sigma_c)^2(1+\sigma_c)} - \frac{1}{Y_s} \frac{(1+\sigma_c)(1-2\sigma_c)(1-2\sigma_s)(1+\sigma_s)}{(1-\sigma_c)^2} + \frac{1}{Y_c} \frac{(1-2\sigma_c)^2(1+\sigma_c)}{(1-\sigma_c)^2} \right] \times \frac{1}{\pi w_0^2},$$ (5)

where d_c is the total thickness of the coating. σ_c and σ_s are the Poisson's ratios and Y_c and Y_s are the Young's moduli of the coating and substrate, respectively. w_0 is the laser beam radius at the mirror. For a multilayer coating, the effective Young's modulus Y_c and Poisson ration σ_c of the coating can be expressed as [16,17]:

$$Y_c = \sum_i Y_i d_i \Big/ \sum_i d_i,$$ (6)

$$\sigma_c = \sum_i \frac{d_i Y_i \sigma_i}{1-\sigma_i^2} \Big/ \sum_i \frac{d_i Y_i}{1-\sigma_i^2},$$ (7)

where d_i, Y_i, and σ_i are the thickness, Young's modulus, and Poisson's ratio of the ith layer, respectively. Substituting Eq. (6) and Eq. (7) into Eq. (4) and Eq. (5), and subsequently into Eq. (3) together with $\phi_B(f)$ and $\phi_S(f)$, $S_x(f)$ can be obtained. The CTN is defined as the square root of $S_x(f)$. $\phi_B(f)$ and $\phi_S(f)$ can be derived from the measured $\phi(f)$ and the calculated U_B, and U_S (see Sec IV).

A CTN model was previously proposed by Harry et al. [18], in which the elastic energy was divided into components parallel and perpendicular to the coating surface with the associated loss angles $\phi_\parallel$ and $\phi_\perp$, respectively. Both energy components are rigorously not independent and may lead to negative energy in certain situations [15]. Hong's and Harry's models lead to the same expression for thermal noise only when $\phi_B = \phi_S$ and $\phi_\parallel = \phi_\perp$ are assumed in each model. For measurements where the information of (ϕ_B, ϕ_S) or ($\phi_\parallel$, $\phi_\perp$) is insufficient, it is often assumed that the components of the loss angles are equal and both models can be used for a first-order estimation of the thermal noise. The CTN in Fig. 6s were calculated by using the rigorous Hong's model except in Fig. 6(d), the red solid curve was calculated under the assumption $\phi_B = \phi_S$ as explained in Sec. IV B.

B. Bulk and shear energy

Strain energy density u of an elastic body is expressed as [19]:

$$u = \frac{1}{2}\sigma_{ij}\varepsilon_{ij}, \tag{8}$$

where σ_{ij} and ε_{ij} are the stress and strain tensors. Both tensors are symmetrical under static equilibrium [19,20]. Expansion of u can be expressed as [20]:

$$u = \frac{1}{2}(\sigma_{11}\varepsilon_{11} + \sigma_{22}\varepsilon_{22} + \sigma_{33}\varepsilon_{33} + 2\sigma_{12}\varepsilon_{12} + 2\sigma_{13}\varepsilon_{13} + 2\sigma_{23}\varepsilon_{23}). \tag{9}$$

Strain and stress tensors are related by the 4th rank stiffness tensor C_{ijkl}:

$$\sigma_{ij} = C_{ijkl}\varepsilon_{kl}. \tag{10}$$

In general, there are only 21 independent elements in C_{ijkl} [21]. For isotropic material such as the amorphous film in our case, only two independent elastic constants remain [21]. Substitute Eq. (10) with the stiffness tensor for the amorphous film, in terms of the bulk modulus K and the shear modulus μ, into Eq. (9), we obtained the energy density for the amorphous film as:

$$u = \frac{1}{2}K(\varepsilon_{11} + \varepsilon_{22} + \varepsilon_{33})^2 + \mu\left[\varepsilon_{11}^2 + \varepsilon_{22}^2 + \varepsilon_{33}^2 + 2(\varepsilon_{12}^2 + \varepsilon_{13}^2 + \varepsilon_{23}^2) - \frac{1}{3}(\varepsilon_{11} + \varepsilon_{22} + \varepsilon_{33})^2\right]. \tag{11}$$

Integrating the energy density over the volume of interest, we can obtain the total energy U:

$$U = U_B + U_S,$$

where

$$U_B = \iiint \frac{1}{2} K (\varepsilon_{11} + \varepsilon_{22} + \varepsilon_{33})^2 dV, \tag{12}$$

$$U_S = \iiint \mu \left[\varepsilon_{11}^2 + \varepsilon_{22}^2 + \varepsilon_{33}^2 + 2(\varepsilon_{12}^2 + \varepsilon_{13}^2 + \varepsilon_{23}^2) - \frac{1}{3}(\varepsilon_{11} + \varepsilon_{22} + \varepsilon_{33})^2 \right] dV. \tag{13}$$

We used the finite element method (FEM), COMSOL 4.4 [22], to obtain the strain tensor ε_{ij} for each element, and together with the known elastic constants K and μ of the film, U_B and U_S can be obtained through the integrations of Eq. (12) and (13). When using the FEM to calculate the energies, mesh sizes need to be optimized to ensure sufficient convergence of the calculated values under the available computational powers. The convergence test was performed by reducing the mesh sizes in our simulation and the optimal mesh sizes were determined such that variations of the values of U_B/U and U_S/U given in Table V were converged to within $\sim 10^{-4}$ range.

C. Temperature-dependence of elastic constants

Temperature dependent Young's modulus and Poisson's ratio of the substrate and the film are required in Eq. (4) and (5) to evaluate the thermal noise for different specifications at different temperature. Table III lists the Young's modulus and Poisson's ratio that we derived from the experimental temperature-dependent stiffness coefficients of silicon [23] for the temperatures of interest. Table III shows that the Young's modulus and Poisson's ratio of silicon are nearly temperature-independent within the temperature range of interest. Equations 4 and 5 indicate that a substrate with a larger Young's modulus, as well as a Poisson's ratio that is close to 0.5, is desirable.. In terms of this consideration, the (111) silicon is preferred for ET-LF and LIGO Voyager. We do not have measurements of the cryogenic Young's modulus and Poisson's ratio for our films, and here we assume that they are also temperature-independent as the silicon.

TABLE III. The temperature dependent Young's modulus and Poisson's ratio for common orientations of silicon derived from the measured stiffness coefficients of silicon from [23].

Temp. (K)	$Y_{[100]}$ (GPa)	$Y_{[110]}$ (GPa)	$Y_{[111]}$ (GPa)	$\sigma_{(111)}$[b]
300	130.1	169.0	187.7	0.262
120	131.1	170.3	189.2	0.263
73	131.1	170.4	189.3	0.263
10[a]	131.1	170.4	189.3	0.264

[a] extrapolate from [23]

[b] on (111) plane of silicon, the Poisson's ratio is isotropic [24].

IV. MECHANICAL LOSS

A.   From cantilever ring-down measurement

The mechanical loss was measured by using the cantilever ring-down method. A cantilever was excited at its vibrational resonant frequency f and the decay time τ of the free-damping was measured. The loss angle of the cantilever $\phi_{can}(f)$ is expressed as

$$\phi_{can}(f) = \frac{1}{Q} = \frac{1}{\pi f \tau},$$

where Q is the quality factor of the cantilever mode.

There are two types of cantilever vibrational modes, namely bending mode and torsional mode, as illustrated in Fig. 1 [25].
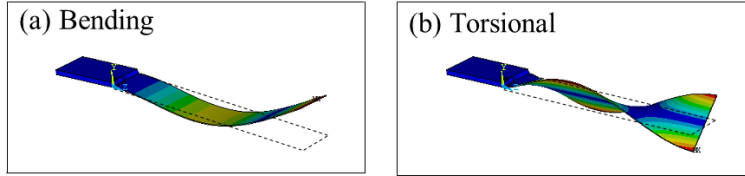

FIG. 1. Illustrations of the vibrational modes of a cantilever in (a) bending mode at 661 Hz and (b) torsional mode at 3642 Hz.

The loss angles of the bare cantilever substrate $\phi_{sub}(f)$ and cantilever with coatings $\phi_{coated}(f)$ are measured and the loss angle of the coating $\phi(f)$ can be derived as

$$\phi(f) = \frac{U_{coated}}{U}\phi_{coated}(f) - \frac{U_{sub}}{U}\phi_{sub}(f), \tag{14}$$

where U_{coated}, U_{sub} and U are the energies of the coated substrate, bare substrate and the coating, respectively. There are two approaches to solve $\phi(f)$ from Eq. (14) if the elastic constants of the substrate and the film are known. One way is to use the analytical approximations for the energies of the bending modes [26] and the torsional modes [27]. The other way is to use the FEM directly to calculate the energies. In addition to giving an exact solution, the latter approach does not require the calculation of elastic constants for the specific orientations with respect to the crystal axes of the sample. We used the FEM approach to obtain the coating loss angle with the elastic constants of the film given in Table II. The elastic constants of the silicon substrate are given in the built-in data base of the FEM software or can be obtained from ref [28].

Cryogenic mechanical losses were measured using the cantilever ring-down method in a cryogenic system [29,30]. The coating loss angles of the single silica film, single silicon nitride film, and 4-pairs and 8-pairs of QW silicon nitride/silica bilayers from 10 K to 130 K are shown

in Fig. 2 for two bending modes at 671 Hz and 1,873 Hz and two torsional modes at 1,221 Hz and 3,755 Hz. Cryogenic loss measurements for the fundamental mode at approximately 100 Hz are usually skipped owing to the long ring-down duration and the high vibrational noise of the cryogenic system at low frequency and low temperature [29]. However, to measure the loss angle at approximately 100 Hz for notable temperatures such as 10 K (for ET-LF), 20 K (for KAGRA), and 120 K (for LIGO Voyager), we turned off the compressor when the desired temperature was reached and the short decay time ($\approx$ 120 s) of the thick coated sample, i.e., 8-pair stack, facilitated the ring-down measurement within the time duration when the temperature rise was negligible. Table IV shows the loss angles for the 109-Hz mode, which was a bending mode, for the 8-pair stack at 10 K, 20 K, and 120 K.
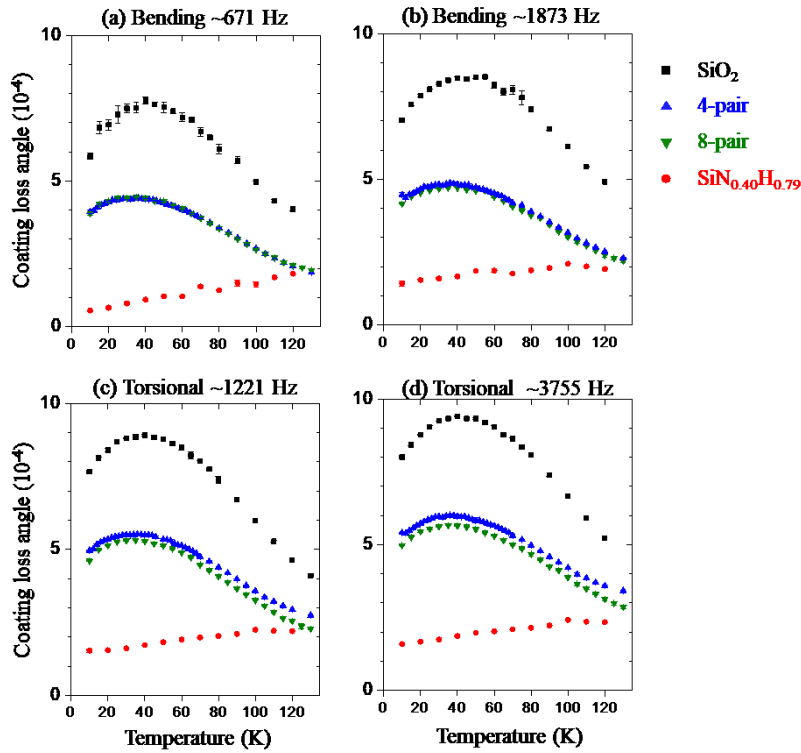

FIG.2. Cryogenic loss angles of the single silica film (black square), single silicon nitride film (red dot), and 4-pairs (blue triangle) and 8-pairs (green triangle) of silicon nitride/silica QW bilayers for bending modes at (a) 671 Hz and (b) 1,873 Hz, and torsional modes at (c) 1,221 Hz and (d) 3,755 Hz.

TABLE IV. Coating loss angles at 10 K, 20 K, and 120 K of the 8-pair silicon nitride/silica QW bilayer for the bending mode at 109 Hz

Temperature (K)	10	20	120
ϕ at 109 Hz (10^{-4})	3.9 ± 0.1	4.4 ± 0.1	2.0 ± 0.1

The room-temperature mechanical loss was measured by using the cantilever ring-down method in a separate system from the cryogenic measurement. Each system has its own limitation on measurement [30,31]. The coating loss angles of the 1-,2-,3-,4-, and 8-pairs of QW silicon nitride/silica bilayer samples are shown in Fig. 3. Theoretically, the coating loss angle of the alternately deposited thin film stack depends only on the thickness ratio rather than the individual layer thicknesses [32]. Therefore, samples with different numbers of QW pairs should ideally have an equal loss angle. The black squares in Fig. 3 represent the average loss angles of these QW stacks. The first two modes were bending modes and the rest were torsional modes.
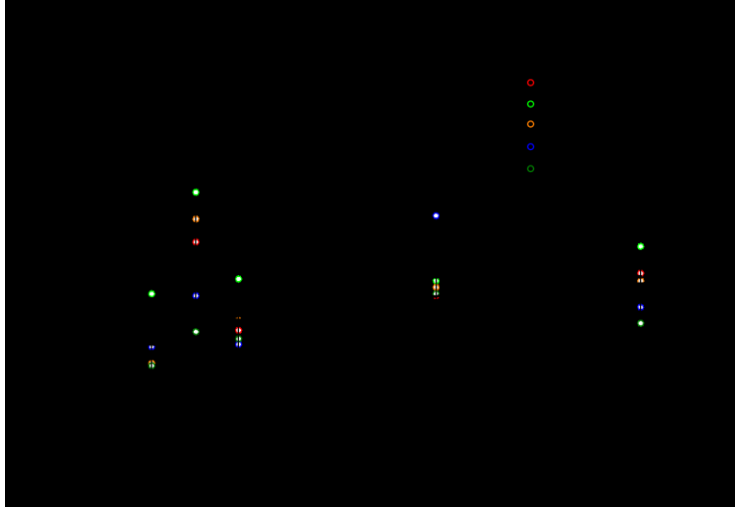

FIG.3 Room-temperature loss angles of the 1-,2-,3-,4-, and 8-pairs of silicon nitride/silica QW bilayer samples. The first two modes were bending modes and the rest were torsional modes. The black solid line is the linear fitting of the averages with error bars.

B.   Bulk and shear loss angles

Equation (2), re-stated here, is used to derive the bulk $\phi_B(f)$ and shear $\phi_S(f)$ loss angles from the measured loss angles $\phi(f)$:

$$\phi(f) = \frac{U_B}{U}\phi_B(f) + \frac{U_S}{U}\phi_S(f).$$
(2)

The normalized energies U_B/U and U_S/U were calculated using the FEM method described in Sec. III B with the following inputs: the cantilever has the thickness of 92 μm and area of 34 mm×5.5 mm. It has a silicon (001) surface, and the long and short axes of the cantilever are along the [$\bar{1}10$] and the [110] direction respectively. The coating consists of 8 silicon nitride/silica QW bilayers with a total thickness of 3.466 μm, and an effective Young's modulus,

Poisson's ratio, and density of 91.6 GPa, 0.206, and 2,104 kg/m^3, respectively, as derived by using Eq. (6) and (7) from the values given in Table II.

TABLE V. FEM results for the normalized bulk and shear energies of the coating

Mode frequency (Hz)	Mode Type	U_B/U (%)	U_S/U (%)
101.5	Bending	26.84	73.16
657.7	Bending	26.78	73.22
1194.2	Torsional	1.18	98.82
1843.1	Bending	26.88	73.12
3613.3	Torsional	2.09	97.91
3634.1	Bending	27.06	72.94
5975.6	Bending	27.29	72.71
6221.6	Torsional	3.75	96.25

Table V shows the FEM results of the normalized bulk and shear energies of the coating for each mode and the mode frequency. It is apparent from Table V that the torsional modes are dominated by the shear motion with negligible bulk energies. According to Eq. (2), the shear loss angle at f_m, $\phi_S(f_m)$, is therefore approximately equal to the measured loss angle, $\phi(f_m)$, of the torsional mode at f_m. $\phi_S(f)$ can therefore be obtained by fitting the $\phi_S(f_m)$ from the torsional modes. The approximation for torsional modes is summarized as:

$$\frac{U_B}{U} \ll \frac{U_S}{U} \qquad \phi_S(f_m) \approx \phi(f_m). \tag{15}$$

Once $\phi_S(f)$ is known, $\phi_B(f_n)$ from the bending mode at f_n can be obtained from Eq. (2) as:

$$\phi_B(f_n) = \frac{U}{U_B}\phi(f_n) - \frac{U_S}{U_B}\phi_S(f_n). \tag{16}$$

The energy ratios can be obtained from FEM. The results are shown in Figs. 4 (a), (b), and (c) for 10 K, 20 K, and 120 K. Linear fits were applied to the loss angle spectra for both the bulk and shear. Figs. 4 reveal that (1) $\phi_B(f)$ is smaller than $\phi_S(f)$, (2) both $\phi_B(f)$ and $\phi_S(f)$ have weak positive frequency dependence, and (3) they are nearly parallel to each other within the range 0 to 5,000 Hz.
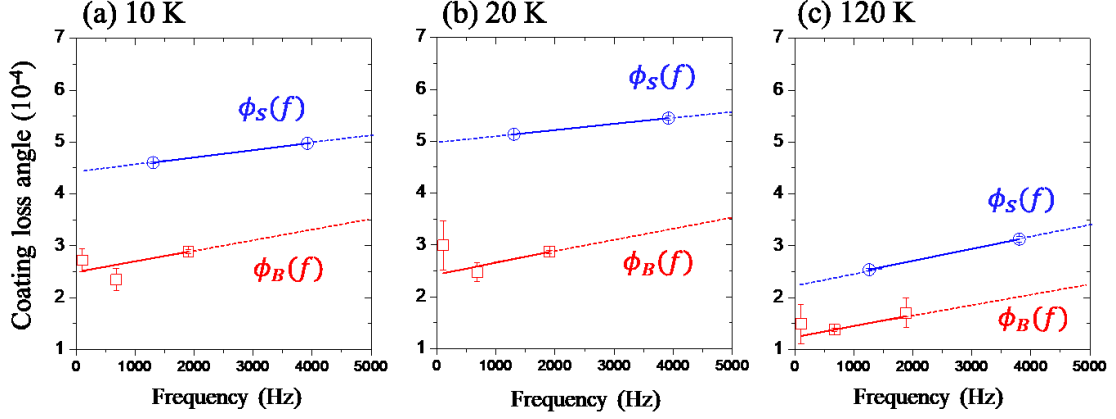
FIG. 4. Bulk and shear coating loss angles at (a) 10 K, (b) 20 K, and (c) 120 K for the silicon nitride/silica bilayer obtained from the 8-pair sample.

For room temperature loss angle, referring to Fig. 3, large uncertainty in the loss angle of the second bending modes leads to $\phi_B(f)$ with an excessively large slope. It is not presently evident how the room-temperature $\phi_B(f)$ would behave in the high-frequency range. Therefore, we assume a single $\phi(f)$, i.e. $\phi_B(f) = \phi_S(f) = \phi(f)$, for the room temperature case as explained in Sec. III A. A linear fit is given to the five measured loss angles as shown in the black solid line in Fig. 3 and it is used for the following room temperature CTN evaluation.

V. COATING THERMAL NOISE EVALUATION

A. Structures for the QW multilayer high reflectors

The structure of the QW multilayer HR, specifically referred to the coating of the end test mirrors (ETMs), should be determined for different specifications listed in Table VI. Hereafter, "H" represents one QW high-refractive-index layer (silicon nitride) and "L" represents one QW low-refractive-index layer (silica), and the "structure" of the multilayer is symbolized as Sub |(LH)^p, e.g., FS |H(LH)^p refers to a structure with one silicon nitride layer (H) adjacent to the fused silica (FS) substrate and p-pairs of silica/silicon nitride (LH)^p on top of it. A design principle to follow is that, for a QW HR stack in air satisfying the specific transmittance requirement with the least number of layers [33,34], the outermost layer must be H and the innermost layer must be the one with the largest refractive index contrast to the substrate such that the phases of the waves reflected from every interface add up constructively to form HR. There is usually a half-wave thick "optical absentee" protection layer on the top and it is skipped here.

TABLE VI. Specifications of the ETM coating for ET-LF, KAGRA, LIGO Voyager, and aLIGO. T is the transmittance and A is the absorption. Y_s and σ_s are the Young's modulus and Poisson's ratio of the substrate, respectively.

Parameter	ET-LF [3]	KAGRA [5]	Voyager [4,9]	aLIGO [9]
Temp. (K)	10	20	120	290
T (ppm)	6	10	5	5
A (ppm)	< 5	0.5-1	≤ 2	< 0.5
λ (nm)	1,550	1,064	1,550	1,064
w_0 (cm)	9.0	4.0	8.4	6.2
CTN[a]	0.9	4.5	2.4	9.2
Substrate	Silicon	Sapphire	Silicon	Fused silica
Y_s (GPa)	189.3[b]	400 [5]	189.2[b]	72 [35]
σ_s	0.26[b]	0.23 [35]	0.26[b]	0.17 [35]

[a] CTN of the whole detector at 100 Hz with the unit in 10^{-21} m/√Hz

[b] for (111) plane from Table III.

We calculated the transmittance and absorption versus the number of layers for the QW HR stack on a substrate by using the Essential Macleod program [22] with the optical constants of silicon nitride and silica films at 1064 nm and 1550 nm given in Table II. The structures satisfying the transmittance requirement for each specification were determined to be: Si $|(LH)^{14}$ for ET-LF and LIGO Voyager, Al_2O_3 $|H(LH)^{13}$ for KAGRA, and FS $|H(LH)^{14}$ for aLIGO. They are shown schematically in Fig. 5 with the relevant parameters. The structures of ET-LF and LIGO Voyager have an absorption of 45.9 ppm. Notably, the extinction coefficient used for the calculation, from Table II, was the room-temperature value. For a semiconductor material such as silicon nitride and amorphous silicon, however, the optical absorption at cryogenic temperature is expected to be lower than that at room temperature owing to the reduced inter-band transition at low temperature. Experimental evidence showed that the absorption coefficient of an amorphous silicon film, which is also a potential high-refractive-index material for the mirror coatings of the next-generation laser interferometer gravitational wave detector, at cryogenic temperature was ≈ 3 times lower than that at room temperature [36]. The thermal-refractive effect, dn/dT, is positive for most of the optical materials. Without knowing the quantitative dn/dT for our films, the physical thickness d_c of the film calculated using the room temperature refractive index will be somewhat under-estimated.
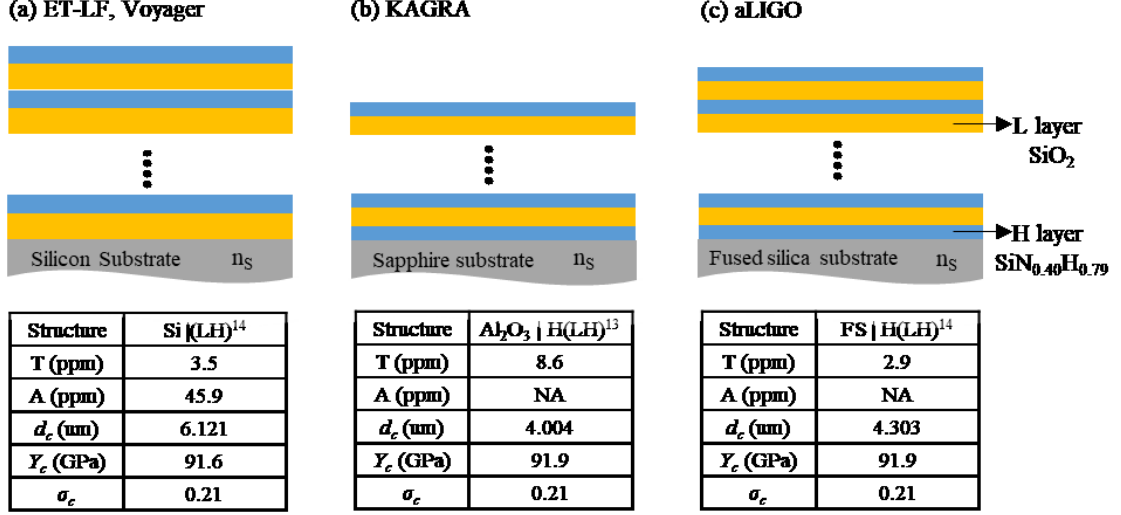
FIG. 5. Schematics of the optimal structures for the ETM coating composed of silicon nitride/silica QW HR stack for (a) ET-LF and LIGO Voyager, (b) KAGRA, and (c) aLIGO, where T and A are the optical transmittance and absorption of the stacks, d_c is the total thickness, Y_c and σ_c are the effective Young's modulus and Poisson's ratio of coating, respectively.

B. Results of thermal noise evaluation

Once the structures are determined, the effective Young's modulus and Poisson's ratio of the coating, Y_c and σ_c, respectively, can be determined from Table II and Eq. (6) and Eq. (7). The results are listed in the tables of Fig. 5 together with the total coating thickness d_c. Substituting all the relevant parameters into Eq. (4) and Eq. (5), U_B / F_0^2 and U_S / F_0^2 can be obtained. Substituting U_B / F_0^2, U_S / F_0^2 together with $\phi_B(f)$ and $\phi_S(f)$ from Fig. 4 and 3 into Eq. (3), CTN of the ETM coatings can thus be obtained. The results are shown in Figs. 6 (a)–(d) as the solid curves.

CTN of the whole detector includes the contributions from the two ETMs and the two input test mirrors (ITMs). It equals to the square root of the sum of two times square of the CTN of the ETM and ITM [37] for un-correlated thermal noise. ITMs have lower transmittance than ETMs and therefore should have less number of layers and hence lower CTN. Without knowing the detail coating structures of the ITMs, CTN of the ETM coating is equal to or greater than one half of the CTN of the whole detector. The lower limits of CTN specification for the coatings of the ETM for ET, KAGRA, LIGO Voyager, and aLIGO are shown in Figs. 6 (a)–(d) as the dash curves. The directly measured CTN of the ETM for the current coating of aLIGO is shown in Fig. 6(d) as the orange dot curve [38]. CTN of the ETM for aLIGO calculated using the coating parameters in Table 5 of Ref. [39], where a single ϕ was assumed for each film, is shown in Fig. 6(d) as the black dot curve.
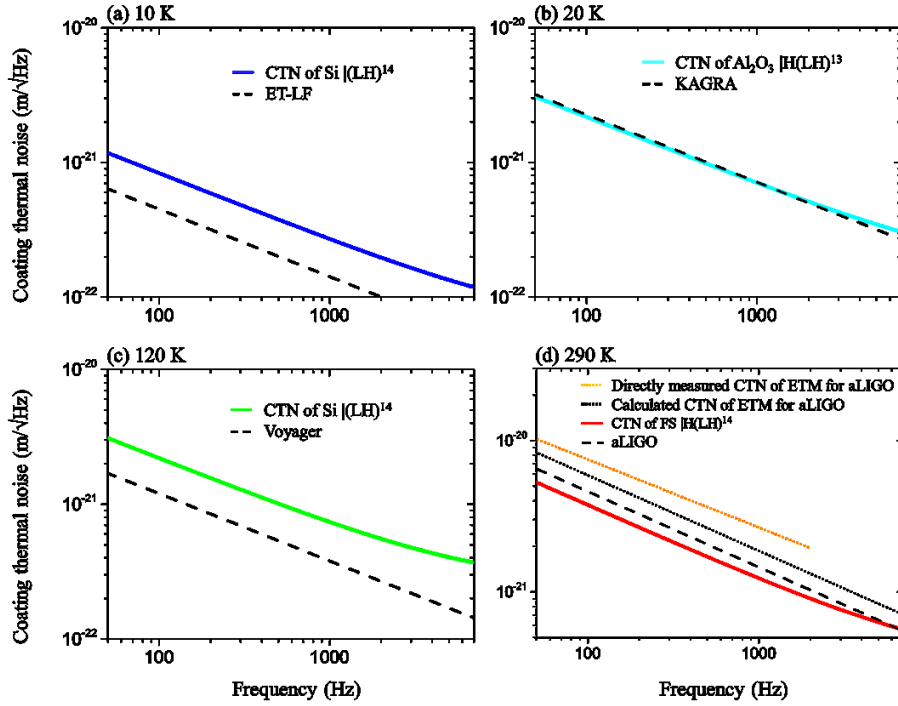
FIG.6. Comparison of the calculated CTN of the silicon nitride/silica QW HR (solid curves) with the lower limit of CTN of the ETM (dash curves) for (a) ET-LF, (b) KAGRA, (c) LIGO Voyager, and (d) aLIGO.

Figure 6 shows that, at 100 Hz, the CTN of the silicon nitride/silica QW HR is 1.8 times higher than the lower limit of the ETM of ET-LF, approximately equal to that of KAGRA, 1.8 times higher than that of LIGO Voyager, and 2 times lower than that of the directly measured CTN of the ETM of aLIGO. Table VII summarizes the transmittance, absorption, and CTN of the silicon nitride/silica QW HR in comparison with the specifications of ET, KAGRA, LIGO Voyager, and aLIGO.

TABLE VII. Summary of the optical transmittance, absorption, and CTN of silicon nitride/silica QW HR and comparison with the specifications of ETM in ET-LF, KAGRA, LIGO Voyager, and aLIGO

ETM	ET-LF		KAGRA		Voyager		aLIGO	
properties	Spec. [3]	Si |(LH)[14]	Spec. [5]	Al$_2$O$_3$ |H(LH)[13]	Spec. [4]	Si |(LH)[14]	Spec. [9]	FS |H(LH)[14]
T (ppm)	6	3.5	10	8.6	5	3.5	5	2.9
A (ppm)	< 5	45.9	0.5–1	NA	≤ 2	45.9	< 0.5	NA
CTN[a]	0.45[b]	0.83	2.25[b]	2.18	1.20[b]	2.20	7.50[c]	3.75

[a] frequency at 100 Hz with the unit in 10^{-21} m/√Hz

[b] lower limit for CTN of the ETM

[c] directly measured CTN of the ETM [38]

14

Both silicon nitride and silica were not subjected to post-deposition heat treatment. It has been shown that the mechanical loss angle of the single silica film can be reduced by varying the deposition temperature and performing post-deposition heat treatment [40]; compatible heat treatment for silicon nitride with silica shall be explored to reduce the mechanical loss of the bilayer and consequently the CTN of the QW HR. Post-deposition heat treatment was also shown to be an effective means to reduce the optical absorption of IBS amorphous silicon [41], and it would be advantageous to explore the effect of thermal annealing on the optical absorption of silicon nitride/silica. The CTN for the current silicon nitride/silica QW HR with respect to the specifications of ET-LF and LIGO Voyager could be improved by implementing the optimized none-QW thickness combination of the silicon nitride and silica layers to minimize the CTN through Eq. (3)–Eq. (7) and maintaining the required transmittance [42,43].

Figure 4 and 3 reveal that all the loss angles of the silicon nitride/silica bilayer have a weakly positive linear frequency dependence within the frequency range of interest as follows:

$$\phi(f) = a + bf, \ a \gg b > 0 . \tag{17}$$

Using the case of room-temperature loss angle to elaborate this effect, we determined that a is 7.41×10^{-5} and b is 6.20×10^{-9} at room temperature from Fig. 3. Substituting Eq. (17) into Eq. (3), it can be shown that the CTN deviates from its normal $1/\sqrt{f}$ dependence and bends asymptotically toward $\sqrt{b \times C}$, where $C = 4 K_B T U / \pi F_0^2$, as illustrated in Fig. 7, with the bend-over frequency defined as a/b. It is evident that a lower loss angle and higher bend-over frequency are desirable in general, i.e., less-dispersive materials with lower loss angle are preferred. For silicon nitride/silica bilayer, the bend-over frequency is 11,962 Hz at room temperature. The coefficients a and b for IBS Ta_2O_5 and IBS silica were presented in Ref. [44]. It can be shown using Eq. (18) that the bend-over frequency for IBS Ta_2O_5/silica is 174,382 Hz at room temperature. Direct measurement of the CTN for the current coatings of aLIGO [38], IBS Ti:Ta_2O_5/silica, within the frequency range 40 Hz to 2000 Hz showed a slope of −0.45 rather than −0.5 for log CTN vs. log f, which also indicates the weakly positive frequency dependence of the loss angle, possibly from the coating materials.
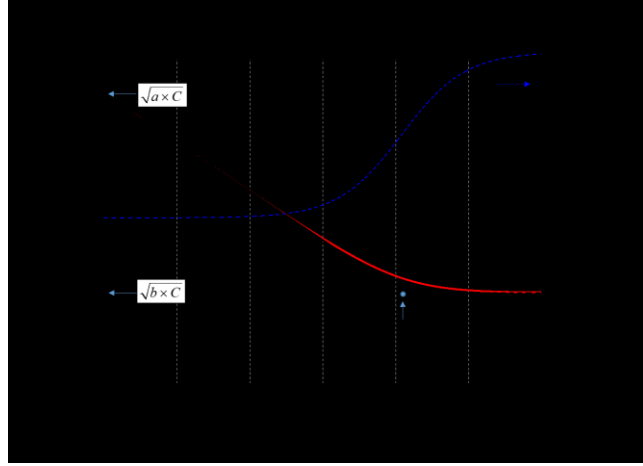
FIG. 7. CTN for silicon nitride/silica QW HR coating with (red solid curve) and without (black solid curve) a linear frequency dependence of the loss angle $\phi(f) = a + bf$. The blue dash curve is the slope of the red curve. $C = 4K_B TU / \pi F_0^2$.

VI. MULTIMATERIAL STACK FOR IMPROVEMENT OF OPTICAL ABSORPTION

Since the standing wave pattern for a QW HR stack peaks at the interfaces of the front few layers (the layers facing the incident beam) and drops rapidly toward the back layers [45], referring to Fig. 8, it was proposed and simulated [46,47] that, for an HL material system with superior mechanical loss but inferior optical absorption such as amorphous silicon/silica [47] and our silicon nitride/silica, the HL stack could be coupled to another stack composed of HL materials with superior optical absorption but inferior mechanical loss, such as the conventional Ti:Ta$_2$O$_5$/silica for aLIGO, in a way that the former is deposited in the back of the HR and the latter is deposited in the front of the HR; the end result is a composite HR stack, referred to as a "multimaterial system," with reduced optical absorption and yet reasonable mechanical loss.
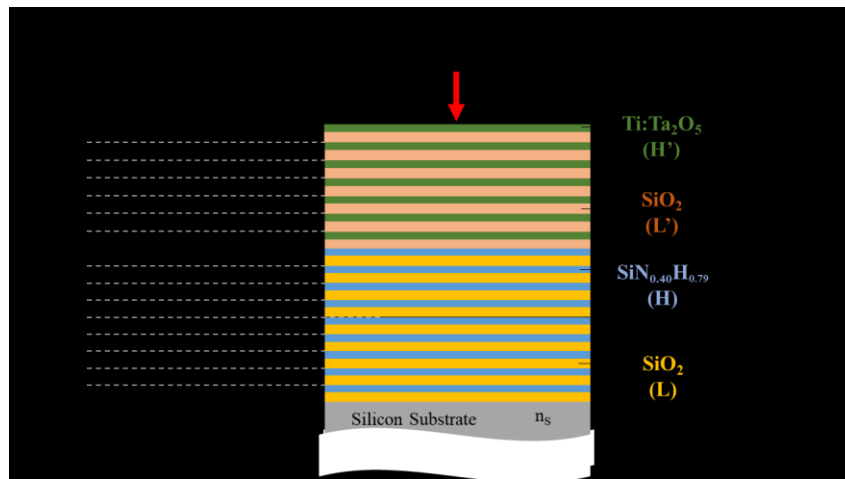

FIG.8. Multimaterial structure. Each layer has QW optical thickness at the wavelength 1550 nm and the total thickness d_c is 7.129 um.

The following optimization for the multimaterial system was specifically aimed for a silicon substrate and the wavelength of 1550 nm, i.e., for ET-LF and LIGO Voyager. In the simulation, we started with the Si |(silica/silicon nitride)[14] PECVD QW HR, referred to as Si |(LH)[14], of the structure in Fig. 5(a). QW pairs of IBS (silica/Ti:Ta$_2$O$_5$) referred to as (L'H'), with the optical constants listed in Table VIII, were added onto the Si |(LH)[14] pair by pair. Optical absorption was calculated for the whole stack after adding each pair. The addition of (L'H') pairs was stopped when the optical absorption reduced to below 2 ppm (the specification of LIGO Voyager). The structure formed up to this point was Si |(LH)[14](L'H')[7]. The (LH) pairs were thereafter removed pair by pair and the transmittance of the whole stack was calculated after the removal of each pair. The removal was stopped when the transmittance increased to no more than 5 ppm. The final structure formed through this process was Si |(LH)[9](L'H')[7] as shown in Fig. 8 schematically. The transmittance was 2.5 ppm and the absorption was 2 ppm. The CTN of the final structure is calculated as follows.

TABLE VIII. Material properties of IBS Ti:Ta$_2$O$_5$ and silica used for multimaterial analysis

Materials	n	κ	Y	Σ	$\phi(10^{-4})$	
	(1550 nm)	(1550 nm) (10^{-7})	(GPa)		10 K	120 K
Ti:Ta$_2$O$_5$[a]	2.05 [48]	5.5[b] [47]	140 [49]	0.23 [49]	4.6 [52]	3.2 [52]
SiO$_2$[a]	1.45 [49]	Negligible [50,51]	72 [49]	0.17 [49]	7 [53]	1.7 [53]

[a] deposited via IBS and annealed at 600°C for 24 h

[b] estimated using the HR absorption in [47] and assuming κ of silica is negligible.

The Young's moduli, Poisson's ratios, and loss angles of the IBS silica and IBS Ti:Ta$_2$O$_5$ were reported in Ref. [49,52,53] and are summarized in Table VIII. Since the loss angles of IBS Ti:Ta$_2$O$_5$ and IBS silica from Ref. [52,53] were not distinguished between the bulk and shear, the CTN for the Si |(LH)[9](L'H')[7] should be calculated by using the CTN model with a single ϕ.

The effective loss angle of (LH)[9](L'H')[7], ϕ, can be obtained by substituting the loss angle, Young's modulus, and thickness of the individual layer from Tables II, IV, and VIII into Eq. (18) given below [32]:

$$\phi = \sum_i \phi_i Y_i d_i \bigg/ \sum_i Y_i d_i . \tag{18}$$

The effective Young's modulus Y_c and Poisson's ratio σ_c of (LH)[9](L'H')[7] can be obtained by the same method described in Section V B. Substituting ϕ, Y_c, σ_c, and the total thickness d_c of (LH)[9](L'H')[7] into Eq. (3)–Eq. (5) by assuming $\phi_B(f) = \phi_S(f) = \phi$, the CTN of Si |(LH)[9](L'H')[7] multimaterial QW HR on a silicon substrate at the wavelength 1550 nm was obtained. The optical transmittance, absorption, and CTN of silicon nitride/silica QW HR and

multimaterial QW HR, and the corresponding specifications of ET-LF and LIGO Voyager are summarized and listed in Table IX for comparison.

Table IX shows that, for the multimaterial Si $|(LH)^9(L'H')^7$, the absorption reduced significantly from 45.9 ppm to 2 ppm and the transmittance remained within the specification. The total thickness of Si $|(LH)^9(L'H')^7$ increased to 7.13 µm as compared with that (6.12 µm) of Si $|(LH)^{14}$, and the CTN at 100 Hz increased about 31% for ET-LF and 28% for LIGO Voyager. A trade-off between the optical absorption and CTN by adjusting the pair numbers of (LH) and (L'H') is possible if the specifications are changed. In general, more (L'H') pairs will give lower optical absorption but higher CTN.

TABLE IX. Comparison of the transmittance, absorption, and CTN between silicon nitride/silica QW HR, multimaterial QW HR, and the specifications of ET-LF and LIGO Voyager

ETM properties	ET-LF			Voyager		
	Spec. [3]	Si $|(LH)^{14}$	Si $|(LH)^9(L'H')^7$	Spec. [4]	Si $|(LH)^{14}$	Si $|(LH)^9(L'H')^7$
T (ppm)	6	3.5	2.5	5	3.5	2.5
A (ppm)	< 5	45.9	2.0	≤ 2	45.9	2.0
CTN[a]	0.45[b]	0.83	1.09	1.20[b]	2.20	2.81

[a] frequency at 100 Hz with the unit in 10^{-21} m/√Hz

[b] lower limit of CTN of the ETM

To realize multimaterial coatings, the deposition sequence of Si $|(LH)^9(L'H')^7$ is designed as follows: (silicon nitride/silica)^9 is deposited continuously in the PECVD chamber on a silicon substrate first and is thereafter moved to the IBS chamber to deposit the (Ti:Ta$_2$O$_5$/silica)^7 stack. Since the optical and mechanical properties of the Ti:Ta$_2$O$_5$/silica QW stack were optimized via post-deposition annealing at 600 °C; therefore, it is expected that the PECVD silicon nitride/silica QW stack should be able to sustain annealing at 600 °C without degradation. It was reported that the amorphous PECVD silicon nitride could sustain annealing up to 800 °C without crystallization [54]. It remains to be seen if the annealing performed at 600 °C on the PECVD silicon nitride/silica stack would improve the characteristics of silicon nitride in terms of absorption and mechanical loss angle as it had improved in the case of amorphous silicon [36,55].

VII. CONCLUSION

In this report, the theories and methods for calculating the thermal noise using Hong's model with bulk and shear loss angles derived from the cantilever ring-down measurement for silicon nitride/silica QW coatings were demonstrated in detail. We have shown that the coating thermal

noise of a QW HR composed of silicon nitride/silica bilayer deposited via the PECVD method are within two times of the lower limit of the ETM for ET-LF and LIGO Voyager and about equal to that of KAGRA. The coatings also showed lower coating thermal noise than that of the current room-temperature detector of aLIGO. The loss angle of the materials showed a linear weakly positive frequency dependence. The optical absorption of the as-deposited silicon nitride/silica QW HR is 45.9 ppm at 1550 nm, which is higher than expected. However, the optical absorption of a multimaterial structure composed of seven pairs of IBS $Ti:Ta_2O_5$/silica and nine pairs of PECVD silicon nitride/silica on a silicon substrate can significantly be reduced to 2 ppm at 1550 nm, which satisfies the specifications of ET-LF and LIGO Voyager. Thermal annealing and optimized layer design are anticipated to further reduce the thermal noise and optical absorption of the silicon nitride/silica HR.

ACKNOWLEDGMENTS

References

[1]   B. P. Abbott *et al*. (LIGO Scientific Collaboration and Virgo Collaboration), Observation of gravitational waves from a binary black hole merger, Phys. Rev. Lett. **116**, 061102 (2016).

[2]   B. P. Abbott *et al*. (LIGO Scientific Collaboration and Virgo Collaboration), GW170817: Observation of gravitational waves from a binary neutron star inspiral, Phys. Rev. Lett. **119**, 161101 (2017).

[3]   ET Science Team, Einstein gravitational wave telescope conceptual design study: ET-0106C-10 (European gravitational observatory, Cascina Italy, 2011) https://tds.virgo-gw.eu/?call_file=ET-0106C-10.pdf

[4]   R. Adhikari *et al*., LIGO III Blue ConceptLIGO, LIGO Report No. LIGO-G1200573, 2012, http://dcc.ligo.org/LIGO-G1200573-v1/public

[5]   K. Somiya, Detector configuration of KAGRA–the Japanese cryogenic gravitational-wave detector, Class. Quantum Grav. **29**, 124007 (2012).

[6]   J. Abadie *et al*. (The LIGO Scientific Collaboration), A gravitational wave observatory operating beyond the quantum shot-noise limit, Nat Phy **7**, 962 (2011).

[7]   J. Aasi *et al*. (The LIGO Scientific Collaboration), Enhanced sensitivity of the LIGO gravitational wave detector by using squeezed states of light, Nat Photonics **7**, 613 (2013).

[8]   H. W. Pan, L. C. Kuo, S. Y. Huang, M. Y. Wu, Y. H. Juang, C. W. Lee, H. C. Chen, T. T. Wen, and S. Chao, Silicon nitride

films fabricated by a plasma-enhanced chemical vapor deposition method for coatings of the laser interferometer gravitational wave detector, Phys. Rev. D **97**, 022004 (2018).

[9] LIGO Scientific Collaboration, Instrument Science White Paper LIGO—T1800133-v4, 2018, https://dcc.ligo.org/LIGO-T1800133/public

[10] H.W. Pan, Z. Z. Xie, L. C. Kuo, and S. Chao, LIGO Report No. LIGO-G1500194, 2015, https://dcc.ligo.org/LIGO-G1500194/public.

[11] B. A. Walmsley, Y. Liu, X. Z. Hu, M. B. Bush, J.M. Dell, and L. Faraone, Poisson's ratio of low-temperature PECVD silicon nitride thin films, J. Microelectromech. Syst. **16**, 622 (2007).

[12] J. Thurn and R. F. Cook, Stress hysteresis during thermal cycling of plasma-enhanced chemical vapor deposited silicon oxide films, J. Appl. Phy. **91**, 1988 (2002).

[13] Y. Levin, Internal thermal noise in the LIGO test masses: A direct approach. Phys. Rev. D **57**, 659 (1998).

[14] H. B. Callen and T. A. Welton, Irreversibility and generalized noise, Phys. Rev. **83**, 34 (1951).

[15] T. Hong, H. Yang, E. K. Gustafson, R. X. Adhikari, and Y. Chen, Brownian thermal noise in multilayer coated mirrors, Phys. Rev. D **87**, 082001 (2013).

[16] R. M. Jones, in *Mechanics of composite materials*, (Philadelphia, Taylor & Francis 1999), ch. 3.2.

[17] K. Srinivasan, Coating Strain Induced Distorsion in LIGO Optics, LIGO Report No. LIGO- T970176-x0, 2017, https://dcc.ligo.org/LIGO-T970176/public

[18] G.M. Harry *et al*., Thermal noise in interferometric gravitational wave detectors due to dielectric optical coatings, Class. Quantum Grav. **19**, 897 (2002).

[19] L. D. Landau and E. M. Lifshitz, *Theory of Elasticity* 3rd edn. (Oxford, Pergamon Press, 1986), ch.1

[20] M. H. Sadd, *Elasticity theory, applications, and numerics* 2nd edn. (Burlington, Academic Press, 2009), ch.6

[21] J. F. Nye, *Physical properties of crystals*. (London, Oxford Press, 1957), ch.VIII.

[22] Thin Film Center, Essential Macleod program. https://www.thinfilmcenter.com/index.php

[23] H. J. McSkimin, Measurement of Elastic Constants at Low Temperatures by Means of Ultrasonic Waves–Data for Silicon and Germanium Single Crystals, and for Fused Silica, J. Appl. Phys. **24**, 988 (1953)

[24] C. H. Cho, Characterization of Young's modulus of silicon versus temperature using a ''beam deflection'' method with a four-point bending fixture, Curr. Appl. Phys. **9**, 538–545 (2009)

[25] W. Y. Wang, Master's thesis, NTHU Hsinchu Taiwan, 2013.

[26] B. Berry and W. C. Pritchet, Vibrating reed internal friction apparatus for films and foils, IBM J. Res. Dev. **19**, 334 (1975).

[27] B. E. White, Jr. and R. O. Pohl, Internal Friction of Subnanometer a-SiO2 Films, Phys. Rev. Lett. **75**, 4437 (1995).

[28] M. A. Hopcroft, W. D. Nix, and T.W. Kenny, What is the Young's modulus of silicon?, J. Microelectromech. Syst. **19**, 229 (2010).

[29] S. Chao, L. C. Kuo, H.W. Pan, C. Cheng, and S. Y. Huang, LIGO Report No. LIGO-G1501048, 2015, https://dcc.ligo.org/LIGO-G1501048/public.

[30] L. C. Kuo, H.W. Pan, H. Wu, H. Y. Ho, and S. Chao, LIGO Report No. LIGO-G1700301, 2017, https://dcc.ligo.org/LIGO-G1700301/public.

[31] H.W. Pan, H. C. Chen, L. C. Kuo, and S. Chao, LIGO Report No. LIGO-G1700299, 2017, https://dcc.ligo.org/LIGO-

G1700299/public.

[32] S. D. Penn *et al.*, Mechanical loss in tantala/silica dielectric mirror coatings. Class. Quant. Grav. **20**, 2917–2928 (2003).

[33] P. W. Baumeister, in *Optical Coating Technology* (Bellingham,SPIE press, 2004), ch. 5.3.1, p. 5–19.

[34] H. A. Macleod, in *Thin-Film Optical Filters* 2nd ed. (Bristol . Hilger, 2001), Ch.5, p. 165.

[35] M. M. Fejer, S. Rowan, G. Cagnoli, D. R. M. Crooks, A. Gretarsson, G.M. Harry, J. Hough, S. D. Penn, P. H. Sneddon, and S. P. Vyatchanin, Thermoelastic dissipation in inhomogeneous media: loss measurements and displacement noise in coated test masses for interferometric gravitational wave detectors, Phys. Rev. D **70**, 082003 (2004)

[36] J. Steinlechner, I. W. Martin, A. S. Bell, J. Hough, M. Fletcher, P. G. Murray, R. Robie, S. Rowan, and R. Schnabel, Silicon-based optical mirror coatings for ultrahigh precision metrology and sensing, Phys. Rev. Lett. **120**, 263602 (2018)

[37] Y. Michimura, K. Komori, A. Nishizawa, H. Takeda, K. Nagano, Y. Enomoto, K. Hayama, K. Somiya, and M. Ando, Particle swarm optimization of the sensitivity of a cryogenic gravitational wave detector, Phys. Rev. D **97**, 122003 (2018)

[38] S. Gras and M. Evans, Direct Measurement of Coating Thermal Noise in Optical Resonators, arXiv:1802.05372.

[39] J. Aasi *et al.* (LIGO Scientific Collaboration), Advanced LIGO, Class. Quantum Grav. **32**, 074001 (2015).

[40] L. C. Kuo, H. W. Pan, H. Wu, H. Y. Ho, and S. Chao, Cryogenic Mechanical Loss of SiO2 film Deposited by Plasma Enhanced Chemical Vapor Deposition Method, LIGO Report No. LIGO- G1700300-v1, 2017. https://dcc.ligo.org/LIGO-G1700300/public

[41] J. Steinlechner *et al.*, Optical absorption of ion-beam sputtered amorphous silicon coatings, Phys. Rev. D **93**, 062005 (2016).

[42] I. M. Pinto, M. Principe, and R. DeSalvo, in *Optical Coatings and Thermal Noise in Precision Measurement*, (Cambridge, New York: Cambridge University Press, 2012),ch. 12.

[43] A. E. Villar, E. D. Black, R. DeSalvo, K. G. Libbrecht, C. Michel, N. Morgado, L. Pinard, I. M. Pinto, V. Pierro, V. Galdi, M. Principe, and I. Taurasi , Measurement of thermal noise in multilayer coatings with optimized layer thickness, Phys. Rev. D **81**, 122001 (2010).

[44] D. R. M. Crooks *et al.*, Experimental measurements of mechanical dissipation associated with dielectric coatings formed using SiO2, Ta2O5 and Al2O3, Class. Quantum Grav. **23**, 4953-4965 (2006).

[45] S. Chao, Y. F. Lin, J. F. Lin, and C. C. Lee, Scattering loss of an optimum pair high reflectance dielectric mirror. Appl. Opt. **29**: 1960–1963(1990)

[46] W. Yam, S. Gras, and M. Evans, Multimaterial coatings with reduced thermal noise. Phys. Rev. D **91**, 042002, (2015).

[47] .J. Steinlechner, I. W. Martin, J. Hough, C. Krüger, S. Rowan, and R. Schnabel, Thermal noise reduction and absorption optimization via multimaterial coatings. Phys. Rev. D **91**, 042001 (2015).

[48] J. Steinlechner and I. W. Martin, High index top layer for multimaterial coatings, Phys. Rev. D **93**, 102001 (2016).

[49] J. Franc, N. Morgado, R. Flaminio, R. Nawrodt, I. Martin, L. Cunningham, A. Cumming, S. Rowan, and J. Hough, Mirror thermal noise in laser interferometer gravitational wave detectors operating at room and cryogenic temperature, arXiv:0912.0107. https://arxiv.org/abs/0912.0107

[50] G. Rempe, R. J. Thompson, and H. J. Kimble, Measurement of ultralow losses in an optical interferometer, Opt. Lett. **17**, 363 (1992)

[51] J. Steinlechner, L. Jensen, C. Krüger, N. Lastzka, S. Steinlechner, and R. Schnabel, Photothermal self-phase-modulation technique for absorption measurements on high-reflective coatings, Appl. Opt. **51**, 1156 (2012).

[52]   I. W. Martin *et al*., Comparison of the temperature dependence of the mechanical dissipation in thin films of Ta2O5 and Ta2O5 doped with TiO2, Class. Quantum Grav. **26**, 155012 (2009).

[53]   I. M. Martin, PhD Thesis, University of Glasgow, 2009.

[54]   N. Jehanathan, M. Saunders, Y. Liu, and J. Dell, Crystallization of silicon nitride thin films synthesized by plasma-enhanced chemical vapour deposition, Scr. Mater. **57**, 739–742, (2007).

[55]   P. G. Murray, I. W. Martin, K. Craig, J. Hough, R. Robie, and S. Rowan, Ion-beam sputtered amorphous silicon films for cryogenic precision measurement systems, Phys. Rev. D **92**, 062001 (2015).